ADVANCED ENERGY MATERIALS
www.advenergymat.de

Low-Concentration Hydrogel Polyelectrolyte with In Situ Formed Interphases Enables 2.7 V Aqueous Pouch Cell

*Tianfeng Qin, Kaiwen Li, Yingjun Liu, Zhen Xu, and Chao Gao**

To maximize energy output, aqueous zinc-based batteries are pushed to extreme potentials far beyond thermodynamic stability limit of aqueous electrolytes. Interphases at interfaces of electrodes/electrolytes are needed to make aqueous batteries stable and reversible kinetically. The absence of interphases at interfaces of hydrogel/electrodes severely impedes aqueous batteries operating in extreme potentials, although low-concentration hydrogels are regarded as promising polyelectrolytes. Herein, a type of initiator system as cross-linking agent is developed that makes hydrogel polyelectrolyte spontaneously in situ form interphases at 25 °C and darkness. This widens the electrochemical stability window of hydrogel polyelectrolyte to above 3.5 V. Also, the initiator system makes the designed hydrogel become a single ion conductor, increasing ionic conductivity to ≈280 mS cm^{-1}. This hydrogel pushes a zinc//$LiMn_2O_4$ pouch cell to operate stably in a voltage window of 0.2 to 2.7 V and deliver high energy densities (e.g., 471 Wh $kg_{LiMn2O4}^{-1}$ at 2.2 $mg_{LiMn2O4}$ cm^{-2}; 203 Wh $kg_{LiMn2O4}^{-1}$, 7.1 $mg_{LiMn2O4}$ cm^{-2}) and excellent rate capabilities (e.g., 410 mAh g^{-1} at 0.11 C, 50 mAh g^{-1} at 57 C, 2.2 $mg_{LiMn2O4}$ cm^{-2}; 175 mAh g^{-1} at 0.7 C, 70 mAh g^{-1} at 7.5 C, and 7.1 $mg_{LiMn2O4}$ cm^{-2}).

1. Introduction

High-energy batteries using organic solvent-based electrolytes are subjected to wide concern due to the increasing demand for electronics powered by electricity.[1] Safety issues impede this process, such as the spontaneous combusting of electric cars in summer.[2,3] Batteries using aqueous electrolytes can circumvent these issues, although exhibit narrow operating voltage windows and corresponding low energy.[4] In order to obtain energy output close or comparable to non-aqueous batteries, aqueous batteries are pushed to work at extreme voltage windows, and these voltage windows are far beyond the thermodynamic stability limit of aqueous electrolytes.[5] None of decomposition by-products from water deposits at interfaces of electrodes/electrolytes to further inhibit hydrolysis (i.e., H_2 and hydroxide at anode, O_2 and H^+ at cathode).[6] It is essential for high-energy aqueous batteries to form interphases kinetically contributing to stability between electrolytes and electrodes as well as reversibility of batteries.

Among different aqueous batteries, zinc-ion batteries (e.g., Zn//$LiMn_2O_4$) draw much attention due to zinc's merits of high volumetric capacity (5855 mAh cm^{-3}), non-toxicity, relatively high abundance, and low cost.[6,7] The willingness that Zn//$LiMn_2O_4$ is to be pushed to extreme voltage windows is strong to maximum energy output. Loose, porous by-product layer of $Zn_4SO_4(OH)_6 \bullet XH_2O$ formed at zinc anode surface cannot further inhibit H_2 evolution, zinc dendrite, or zinc corrosion reaction.[8] In order to negatively widen the anodic potential limit of zinc and solve the above issues, much effort in constructing solid electrolyte interphases (SEI) has been made firstly. Inorganics, organics, and inorganics/organics hybrids SEI are adhered on zinc surfaces through blade coating, in situ interfaces reactions, electrolyte additive engineering.[6,9–11] These artificial built SEI layers suffer from degradation or cracking after repeated zinc plating/striping accompanied by volume change.[9] Corresponding Zn//$LiMn_2O_4$ operates in the voltage windows below 2 V.[12–14] Cathodic electrolyte interphase (CEI) can guarantee transition metal oxide cathodes operate reversibly in high cathodic potential limit by further avoiding hydrolysis. Unfortunately, CEI is seldom reported in aqueous Zn//$LiMn_2O_4$ system and others. The absence of CEI at the interface of electrolyte/cathode may be one of the reasons that voltage window is below 2 V. CEI is not observed in 2.3 V Zn//$LiMn_2O_4$ system based on advanced water-in-salt and deep eutectic electrolytes.[15] In order to push aqueous Zn//$LiMn_2O_4$ to extreme potentials, it is meaningful to spontaneously in situ form robust SEI and CEI in assembled batteries.

Organic molecular electrolyte additives can contact both anodes and cathodes simultaneously, but lack the ability to form CEI and robust SEI. Residual monomers in hydrogels can be used as one of the promising additives, where their polymers polymerized at electrode/electrolyte can minimize the content of free water and thus widen the electrochemical stability window.[16,17] For the hydrogels based on free radical

T. Qin, K. Li, Y. Liu, Z. Xu, C. Gao
MOE Key Laboratory of Macromolecular Synthesis and Functionalization
Department of Polymer Science and Engineering
International Research Center for X Polymers
Key Laboratory of Adsorption and Separation Materials and Technologies of Zhejiang Province
Zhejiang University
Hangzhou 310027, China
E-mail: chaogao@zju.edu.cn

The ORCID identification number(s) for the author(s) of this article can be found under https://doi.org/10.1002/aenm.202300733

DOI: 10.1002/aenm.202300733

polymerization, the degree of polymerization can be increased rapidly to 10^3–10^4 within 0.1–10 seconds in the chain growth elementary reaction.[18,19] The rapid chain growth makes the prepared hydrogels contain only polymers and residual monomers.[18,19] Residual monomers are derived from the disproportion termination (polymerization temperature is above 60 °C) and the chain transfer.[18,19] For example, polyacrylamide hydrogel through free radical polymerization contains only polyacrylamide and residual acrylamide monomers. But polyacrylamide hydrogel exhibits a narrow electrochemical stability window, especially poorly tolerant to high voltage. On the one hand, polyacrylamide is inert due to unmatched highest Occupied Molecular Orbital (HOMO) and lowest unoccupied molecular orbital (LUMO) with Fermi energy levels of electrodes in $Zn//LiMn_2O_4$,[20–22] and thus no interphase is formed at the interface of electrode/electrolyte. On the other hand, residual monomers cannot be polymerized to form interphase at the interface of electrode/electrolyte in assembled batteries, due to exhausted active free radical from the thermal decomposition of persulfate. Current initiation system for free radical polymerization generates active free radical under heating or high-energy radiation irradiation, rather than at room temperature and darkness, which limits the in situ formation and self-repair of interphases at interfaces of electrode/hydrogel polyelectrolyte in assembled batteries. It is necessary to develop a type of initiator system that can generate active free radical in a controlled and continuous manner.

Herein, by developing a novel initiator system based on polycations chemistry, we report a high-voltage hydrogel polyelectrolyte with high-conductivity. The developed initiator system as cross-linking agent can generate radicals to initiate monomers in a controlled and continuous manner. The developed initiator system can, on the one hand, generate active free radical to initiate monomers to form hydrogel polyelectrolyte at 70 °C; on the other hand, produce active free radical to initiate residual monomers at room temperature and darkness. The latter insures the in situ formation and self-repair of interphases (i.e., SEI and CEI) at interfaces of electrodes/hydrogel polyelectrolytes in assembled batteries. This widens the operating voltage windows of hydrogel polyelectrolyte (above 3.5 V) and aqueous batteries (0.2–2.7 V). In addition, the developed initiator system makes hydrogel become a single ion conductor with high ionic conductivity (≈280 mS cm^{-1} at 25 °C). Dual cross-linking polyacrylamide hydrogel-based electrolytes make $Zn//LiMn_2O_4$ pouch cell (2.2 mg cm^{-2}, $LiMn_2O_4$) operate in the voltage window of 0.2–2.3 V, exhibiting high energy density (471 Wh $kg_{LiMn2O4}{}^{-1}$) and excellent cycling stability (300 mAh g^{-1} after 240 cycles at 0.35 C) as well as high rate capability (410 mAh g^{-1} at 0.11 C; 50 mAh g^{-1} at 57 C). Also, dual initiation and dual cross-linking polyacrylamide hydrogel (DPH)-based electrolyte can make $Zn//LiMn_2O_4$ pouch cell (7.1 mg cm^{-2}, $LiMn_2O_4$) operate in the voltage window of 0.2–2.7 V, delivering high energy density (203 Wh $kg_{LiMn2O4}{}^{-1}$) and excellent cycling stability (145 mAh g^{-1} after 320 cycles at 1.81 C) as well as good rate capability (175 mAh g^{-1} at 0.7 C; 70 mAh g^{-1} at 7.5 C).

2. Results and Discussion

2.1. Radicals Formation Mechanism of Initiator System Based on Aluminum Polycations

Aqueous aluminum chemistry has been studied for one century at least due to its importance and complexity.[23] Al^{3+} exists in the form of monomeric cations, polymeric cations (polycations), or others.[24] In partially neutralized Al^{3+} solution, pH, the ratio of OH^-/Al^{3+}, aging, concentration, and so on have an important influence on the hydrolysis-polymerization of aluminum.[25] And these have been studied by many researchers using base titration, Ferron method, ^{27}Al NMR, and so on.[26–28] It is exciting that hydroxyl and sulfate radicals (HO, $SO_4{}^-$) are formed in our aluminum polycations(PC) aqueous solution. Corresponding mechanism is related to the shift of vibration energy levels (E_V) and the decrease of changed dipole moment (**Δμ**) of bonds in PC, especially for O–H stretching vibration of H_2O in H_2O–Al.

As for our research, forced hydrolysis of 0.36 M $Al_2(SO_4)_3$ solution is carried out to form aluminum polycations solution (OH^-/Al^{3+} = ≈2.2, pH ≈4.2). Aging is made at room temperature (25 °C) and heating at 70 °C for different time (e.g., 20 min; 2, 6, and 48 h).^{27}Al MAS NMR, XRD, and FTIR measurements are used to monitor the aging process as shown in Figures S2–S8 (Supporting Information). As the aging of PC (aluminum polycations) continues, the content of monomers, oligomers, medium, and high polymers varied regularly as shown in Figure S9a (Supporting Information). Correspondingly, wavenumbers of bonds' vibration in PC also shift regularly in Figure S9b (Supporting Information), where wavenumber is equal to frequency/(light velocity). According to the quantum mechanics theory (i.e., quantization of vibrational energy level), frequency is related to the vibration energy level of bonds as shown in Figure S7 (Supporting Information) (text description). We find the regular shift of vibration energy level of bonds in PC as shown in Figure S9c (Supporting Information). Absorbance (A) is related to (**Δμ**).[2] As the aging process continues, the value of absorbance differential decreases as shown in Figure S10b (Supporting Information).

The transformation of different polycations is shown in **Figure 1**a. For pure $Al_2(SO_4)_3$ aqueous solution, hydrolysis occurs and the majority of aluminum specie is $[Al(OH_2)_6]^{3+}$, where pH is ≈2.58. After adding NaOH plates into 0.36 M $Al_2(SO_4)_3$ aqueous solution, the hydrolysis-polymerization-dissolution of aluminum polycations is initiated as shown in Figure 1a. During the transformation processes of aluminum species, the shift of E**V** and the decreased **Δμ** of bonds result in the formation of hydroxyl radicals. Heating, as one of aging methods, can accelerate the transformation processes from the viewpoint of kinetics, resulting in the increase of radicals concentration. When the aging process at 70 °C continues to 48 h, excluding precipitations, only $[Al_{30}O_8(OH)_{56}(OH_2)_{10}]^{18+}$ (Al30) and $[Al(OH_2)_6]^{3+}$ (Al1) are detected. During the whole transformation process, hydroxyl radicals at different time sites are detected as shown in Figure S12 (Supporting Information). Radicals concentration in **Figure 2**b varies regularly during the whole aging process, where hydroxyl

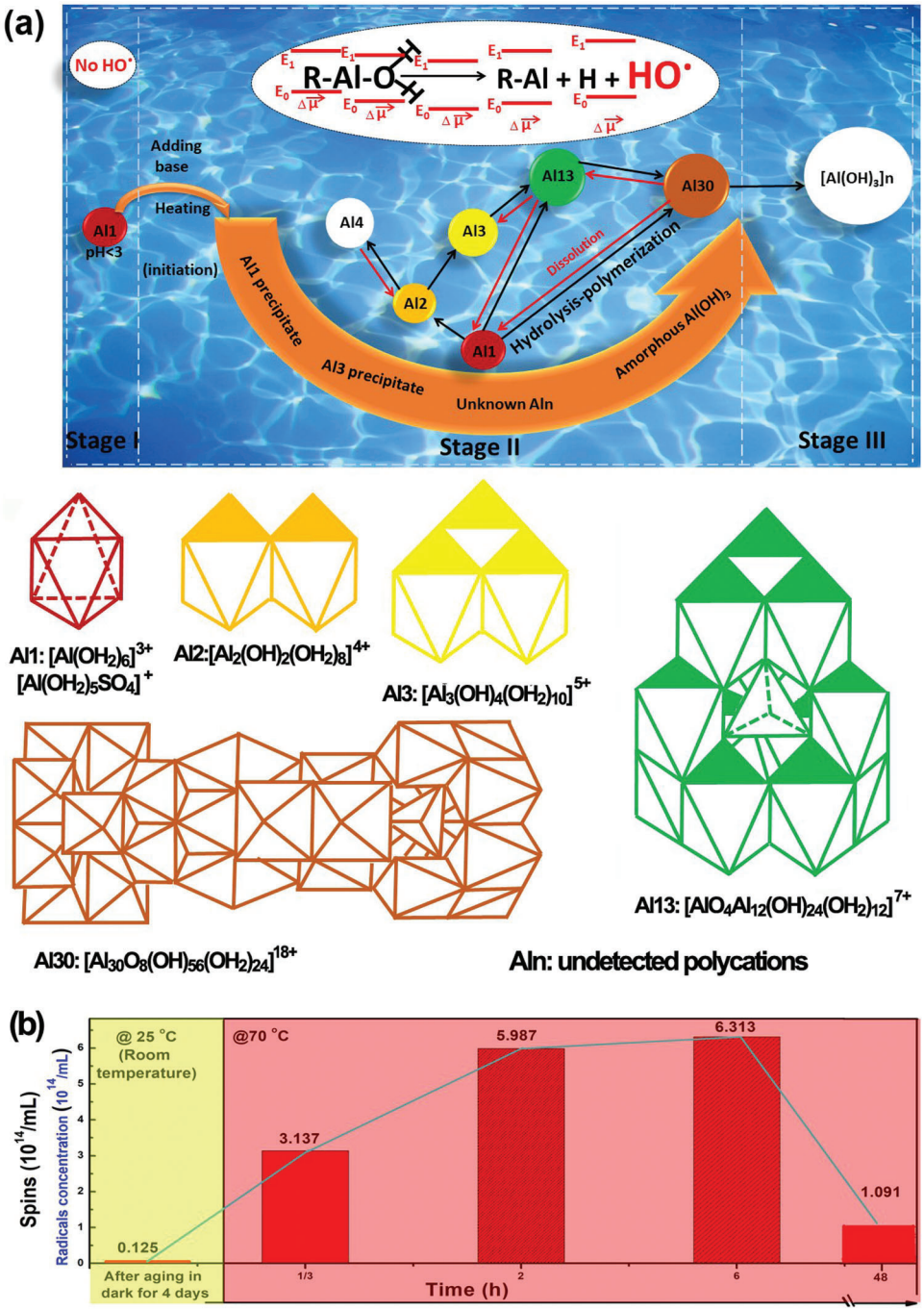

Figure 1. a) Transformation pathways of aluminum polycations with the continuing of aging process. b) Hydroxyl radicals concentration as a function of aging time.

radicals concentration is based on quantitative results of electron paramagnetic resonance (EPR) in Figure S12 (Supporting Information). By fitting, we find that radicals concentration differential (y) is related to absorbance differential (x) of bond vibrations in PC (i.e., $y = \text{intercept}+B1X+B2X^2+B3X^3$), as shown in Figure S11 (Supporting Information).

With the purpose of designing high-voltage high-conductivity polyelectrolyte, PC is directly used as initiator and cross-linking agent to prepare hydrogel at room temperature in dark. After half of a month, as shown in Figure S13b (Supporting Information), a round cake-shape white polyacrylamide hydrogel forms in the bottom of beaker; poor cross-linking white polyacrylamide in Figure S13 (Supporting Information) (a, upper) produces on the top of round cake-shape hydrogel. It is exciting that the whole PC containing acrylamide monomers become a white solid-state hydrogel monolith (PAAmPCH) after heating at 70 °C for ≈30 min.

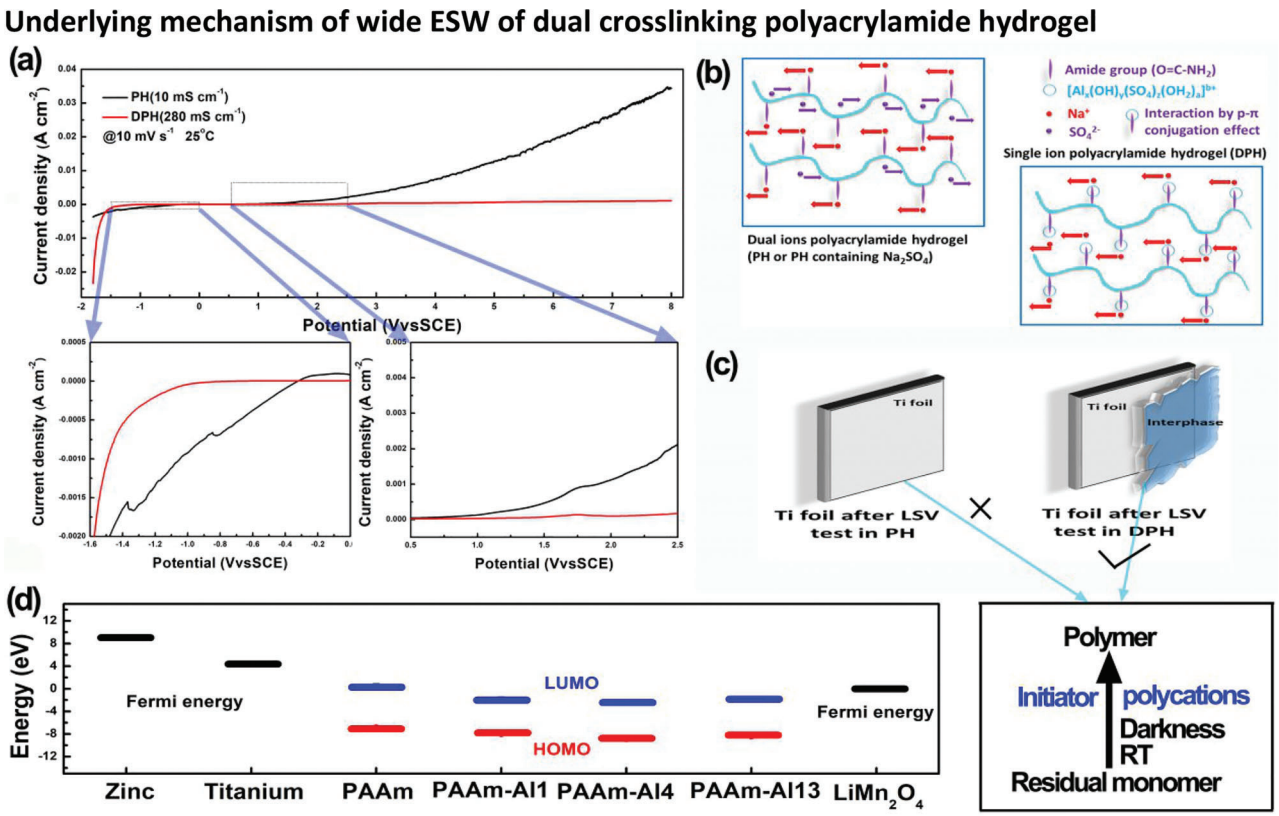

Figure 2. a) LSV curves of DPH and PH polyelectrolytes, Ti foil as working electrodes and Pt as counter electrodes. Schematic diagram of b) ions diffusion in polyelectrolytes and c) Ti foil electrodes tested in polyelectrolytes (RT: room temperature). d) Fermi energy of electrodes (e.g., zinc, titanium, $LiMn_2O_4$), and LUMO&HOMO of polyacrylamide (PAAm), PAAm-Al1, PAAm-Al4, and PAAm-Al13.

A piece of PAAmPCH is shown in Figure S14a,b (Supporting Information). This is due to the initiation of radicals and the cross-linking of aluminum polycations in PC. As a control, aqueous solution only containing acrylamide monomers do not become a solid-state hydrogel even after heating at 70 °C for 6 h, as shown in Figure S14c,d (Supporting Information). A piece of PAAmPCH is soaked into 2 M H_2SO_4 aqueous solution to investigate the cross-linking nature, as shown in Figure S14e1–e3,f1–f3 (Supporting Information). After 7.5 h, PAAmPCH becomes transparent in Figure S17f1,f2 (Supporting Information). The transparent PAAmPCH become poor cross-linking nature in Figure S14f3 (Supporting Information), demonstrating the function of polycations as physical cross-linking agent. PAAmPCH exhibits porous network structure and excellent strength in Figure S15 (Supporting Information). XPS, FTIR, Raman, and XRD characterizations are shown in Figures S16 and S17 (Supporting Information). Corresponding results are consistent with other reported hydrogels prepared with KPS and MBA, excluding SO_4^{2-}, SO_3^{2-}, and Al polycations. And thus descriptions are not made.

After PC aging at 70 °C for 48 h and cooling to 25 °C, acrylamide monomers are added, which does not form solid-state hydrogel but white flowing liquid under 70 °C for 6 h in Figure S18 (Supporting Information). Inert gas (N_2) is used to saturate PC, with the purpose of eliminating air and investigating the initiation mechanism. EPR spectra are collected to observe the difference before and after saturating with N_2. As shown in Figure S19a (Supporting Information), PC saturated with N_2 exhibits poor hydroxyl radicals signal peaks at 25 °C in dark. When heating at 70 °C for 20 min, PC saturated with N_2 exhibits strong hydroxyl and sulfate radicals signal peaks in Figure S19b (Supporting Information). Acrylamide monomers are initiated and cross-linked by PC, forming white hydrogel in Figure S19c (Supporting Information). And corresponding radicals concentration is up to 5.394×10^{14} mL^{-1} in Figure S19b (Supporting Information), which is 1.7 times higher than that of PC without N_2 saturation (3.137×10^{14} mL^{-1}) in Figure 1b. As shown in Figure S12e (Supporting Information), HO (hydroxyl radicals) is observed in EPR spectrum of PC aging at 70 °C for 48 h, but sulfate radicals signal peak is not observed. It can be inferred that the initiation of acrylamide monomers is ascribed to sulfate radicals. FTIR characteristic bands of SO_4^{2-}/SO_3^{2-} at ≈1100 cm^{-1} are fitted as shown in Figure S20a–e (Supporting Information).[29] With the aging process continuing, the relative content of SO_4^{2-} gradually decreases; the relative content of SO_3^{2-} increase, as shown in Figure S20f (Supporting Information). SO_3^{2-} is derived from transition reaction of sulfate radicals, which is demonstrated by S2p XPS spectra in Figure S20g (Supporting Information) including text and reaction descriptions.

Radicals formation of PC is derived from the shift of E_V and the decreased $\Delta\mu$ (X) of intermediates during the aging processes. Correspondingly possible mechanism on radicals formation is as

the words and equations after Figure S18 (Supporting Information). Low-concentrated $Al_2(SO_4)_3$ aqueous solution (0.002 M) is used to demonstrate the conclusion. With the aging continuing, radicals concentration, and signal peak gradually increase and become strong, respectively, as shown in Figure S21 (Supporting Information). Acrylamide monomers dissolved into 0.002 M $Al_2(SO_4)_3$ aqueous solution is initiated and cross-linked to form transparent hydrogel after heating at 70 °C for at least 3 h, as shown in Figure S22a. The mass of $Al_2(SO_4)_3$ is equal to the total mass of common initiator potassium peroxodisulfate (KPS) and cross-linking agent N-methylene diacrylamide (MBA) (57.5 mg in 60 mL water containing 8.68 mg acrylamide), demonstrating the dual functions of PC. Also, acrylamide monomers dissolved into $Al(ClO_4)_3$ and $Al(NO_3)$ aqueous solutions, respectively, form transparent hydrogels after heating at 70 °C for at least 3 h, as shown in Figure S22b,c (Supporting Information).

2.2. Underlying Mechanism of Wide ESW of Dual Cross-linking Polyacrylamide Hydrogel

Achieving high-voltage high-conductivity low-concentration hydrogels electrolytes is the goal of high-energy, safe, environmental friendly batteries. Reported polyacrylamide hydrogels (PH) are prepared by using an initiator (e.g., $K_2S_2O_8$) and cross-linking agent (e.g., MBA) under heating.[30] PC, as the second initiator and cross-linking agent, is introduced to obtain DPH. Fourier Transform Infrared Spectroscopy (FTIR) and X-ray photoelectron spectroscopy (XPS) data are collected to investigate the physical-chemical properties of PH and DPH, as shown in Figure S23 (Supporting Information). Characteristic peaks of DPH exhibit much stronger absorbance due to larger change of dipole moment of bonds, as shown in Figure S23a (Supporting Information). The results of XPS also manifest the existence of aluminum polycations in DPH, in Figure S23b–l (Supporting Information).

Stress–strain curves are collected as shown in Figure S24 (Supporting Information). Strength and elongation decrease largely after adding 1 M Na_2SO_4 into polyacrylamide hydrogel, $PH(Na_2SO_4)$. Aluminum polycations do not affect the strength and elongation of DPH, and thus it is suitable for battery separators. Linear sweep voltammetry curve (LSV) measurement is carried out to investigate the possibility of DPH as electrolytes for high-energy batteries. As shown in Figure 2, LSV curve of DPH exhibits the cathodic potential limiting above 2.5 V, and the anodic potential limiting below −1 V. Electrochemical stability window (ESW) of DPH is expanded to above 3.5 V, wider than that of PH (≈1 V, −0.25 to 0.75 V). Ionic conductivity of DPH is up to ≈280 mS cm^{-1} in Figure 2, much higher than those of PH (10 mS cm^{-1}) and PH containing 1 M Na_2SO_4 (103 mS cm^{-1} in Figure S1, Supporting Information).

High-voltage high-conductivity mechanisms are elucidated. LSV curve of polyacrylamide hydrogel (PAAmPCH) that monomers are initiated and cross-linked by PC is collected as shown in Figure S25 (Supporting Information). Electrochemical stability window (ESW) and ionic conductivity of PAAmPCH are above 3.5 V and ≈293 mS cm^{-1}, respectively. One can conclude that wide ESW and high ionic conductivity are related to PAAmPCH. Thus, PH and DPH are investigated comparatively.

^{27}Al MAS NMR is used to detect the type of aluminum polycations of DPH freeze drying (FD). As shown in Figure S26 (Supporting Information), monomer $[Al(OH_2)_5SO_4]^+$, tetramer $[Al_4(OH)_6(OH_2)_{12}]^{6+}$, tridecamer $[AlO_4Al_{12}(OH)_{24}(OH_2)_{12}]^{7+}$ are detected. The content of monomer $[Al(OH_2)_5SO_4]^+$ is up to 68%. A mass of SO_4^{2-} and the whole OH^- are accepted by Lewis acid Al^{3+} to form polycations. Polycations as physical cross-linking agents interact with the amide group by strong coulombic force in Figure S28 (Supporting Information). Thus, DPH is a single sodium ion conductor, exhibiting a high ionic conductivity, in the right part of Figure 2b. PH containing 1 M Na_2SO_4 and PH are dual ions conductor (i.e., Na^+ and SO_4^{2-} conductors), resulting in moderate ionic conductivities, in the left part of Figure 2b.

A mass of free H_2O is accepted as structural water, forming aluminum polycations. The content of free water in DPH decreases remarkably. Interphase is formed at interface of Ti foil electrode/DPH electrolyte, and XPS measurement is carried out to get the information on interphase. As shown in Figure S27a (Supporting Information), the titanium content of Ti foil electrode after LSV test in DPH decreases to ≈1.08 at% due to the formation of interphase at Ti surface in the right part of Figure 2c, much lower than that of one in PH (8.24 at%). The nitrogen content of Ti foil electrode after LSV test in DPH is much higher than that of one in PH. Based on XPS narrow spectra in Figure S27b–k (Supporting Information), the interphase is composed of inorganics and organics, deriving from DPH derivatives. Interphase does not form at the surface of Ti foil electrode after LSV test in PH, in the left part of Figure 2c.

For polyacrylamide hydrogel through radicals polymerization, residual acrylamide monomer is unsaturated organic additives (as shown in Radicals polymerization of Part two, in supplementary information).[18,19] Due to exhausted radicals in PH, residual acrylamide monomer cannot be polymerized into polyacrylamide film adhered on Ti surface. On the contrary, the developed initiator system in DPH can generate active radicals at room temperature and darkness to polymerize residual acrylamide monomer into polymer, which is also demonstrated by Figure S13 (Supporting Information). Interphase is formed at the interface of Ti foil/DPH. Besides, according to reported literature, the formation of SEI on the anode or CEl on the cathode is related to Fermi energy level of electrodes and LUMO&HOMO of electrolytes.[21] Simulation computation on HOMO and LUMO of polyacrylamide and its composites is carried out as shown in Figure S28 (Supporting Information). Fermi energy of titanium is ≈4.42 eV,[31] which is larger than these of LUMO of polyacrylamide and polyacrylamide-Aln (n = 1, 4, and 13) in Figure S28 (Supporting Information) and Figure 2d. SEI should be formed at Ti electrode surface as supposed. But anodic potential limiting of PH is not widened compared to one of DPH. One can conclude that SEI is formed at surface of Ti electrode after LSV test in DPH, not in PH. The reason of SEI formation is due to our developed initiator system that can generate radicals to polymerize monomer at room temperature and darkness. Fermi energy of titanium is ≈4.42 eV, larger than these of HOMO of polyacrylamide and polyacrylamide-Aln in Figure S28 (Supporting Information) and Figure 2d. It is impossible to form CEI at Ti electrode surface. Compared to PH, cathodic potential limit of DPH is widened due to our developed initiator system that can generate radicals to polymerize monomer at room temperature and

darkness. It is also predicted that residual acrylamide monomer in hydrogel can be polymerized at surface of electrode (e.g., zinc anode, $LiMn_2O_4$) to form SEI and CEI by our developed initiator system.

2.3. Charge Storage Mechanism of High-Voltage Zn//$LiMn_2O_4$ Based on DPH Polyelectrolyte

ESWs of hydrogels containing $ZnSO_4$ (Zn) are evaluated first by LSV measurement. As shown in Figure S29a (Supporting Information), ESW of PH(Zn) is not widened, excluding zinc plating/stripping peaks. Carrageenan (C) is added to increase strength.[32] Corresponding LSV curve of PH containing C [PH(C)] in Figure S29b (Supporting Information) exhibits a lower anodic potential limiting but poor tolerance to high potential. DPH containing Zn and C [DPH(CZn)] exhibits decreased anodic polarization current and expanded cathodic potential limiting. Ionic conductivity of DPH(CZn) is 88 mS cm^{-2}, higher than that of PH(Zn) in Figure S29a (Supporting Information), even if C increasing viscosity is added.

Voltage profiles of Zn//Zn coin cells are collected to study the effect of the designed polyelectrolyte on zinc plating/stripping. As shown in Figure S30 (Supporting Information), DPH(CZn) polyelectrolyte makes zinc plating/stripping stably even after ≈4000 h. Cumulative capacity of zinc plating/stripping is up to 2200 mAh cm^{-2}. Zn//Zn coin cell based on PH(Zn) polyelectrolyte exhibits larger over-potential after 50 h, and becomes short circuit after 1500 h. SEM measurement is carried out to observe the morphology variations of Zn foil electrodes after plating/stripping cycles (0.2 mA cm^{-2}, 0.2mAh cm^{-2}), as shown in Figure S31 (Supporting Information). For cycled Zn//Zn coin cell based on DPH(CZn), surface of zinc foil electrode is smooth in SEM image of Figure S31a (Supporting Information). Surface crack of zinc foil electrode is also found, as shown in Figure S31b (Supporting Information), in which the surface crack is derived from tearing DPH(CZn) polyelectrolyte adhered onto zinc foil electrode. Cross-section of Zn foil electrode is composed of two layers that one is zinc foil; the other is solid electrolyte interphase (SEI). For cycled Zn//Zn based on PH(Zn), the surface of zinc foil electrode becomes porous and produces a number of flake-shape by-products, as shown in Figure S31d (Supporting Information). XRD patterns are collected to investigate phase variations of Zn foil electrodes after plating/stripping cycles (0.2 mA cm^{-2}, 0.2 mAh cm^{-2}), as shown in Figure S31e (Supporting Information). For cycled Zn//Zn based on DPH(CZn), obvious signal peaks appear in XRD pattern of zinc foil electrode, which are indexed to zinc metal (PDF#04-0831). For cycled Zn//Zn based on PH(Zn), excluding zinc peaks, extra signal peaks are observed and indexed to $Zn_4SO_4(OH)_6{\bullet}5H_2O$ (PDF#39-0688). $Zn_4SO_4(OH)_6{\bullet}5H_2O$ (ZSH) is the main by-product generated due to hydrogen evolution reaction (HER) followed by a local pH increase.[33,34] PH(Zn) does not inhibit HER at the interface of zinc anode/polyelectrolyte. On the contrary, DPH(CZn) can inhibit HER due to the formation of SEI that avoids the contact between H_2O and zinc anode. Zinc preferred growth orientation is different as shown in Figure S31e (Supporting Information). For Zn//Zn based on DPH(CZn), zinc preferred growth orientation is along (002) crystal face, which inhibits zinc dendritic growth; For Zn//Zn based on PH(Zn), it is (101) crystal face, which does not. From interphase composition of Ti foil electrode, it can be known that SEI of zinc anode is composed of inorganics and organics, deriving from DPH(CZn) derivatives. Especially, SO_3^{2-} groups are reported as zincophilic sites, which uniformizes the zinc ions flux and transport.[33] SEI containing SO_3^{2-} groups induces zinc preferred growth orientation to (002), inhibiting zinc dendritic growth.[35,36]

Zn//$LiMn_2O_4$ coin cells are selected as models to demonstrate the tolerance of designed polyelectrolytes to high-voltage window. In order to inhibit manganese ions dissolution of $LiMn_2O_4$, Mn^{2+} is introduced into DPH(CZn), i.e., DPH(CZnMn).[37] In our PC, Mn^{2+} replaces Al^{3+} of AlO_4 tetrahedron in $[AlO_4Al_{12}(OH)_{24}(OH_2)_{12}]^{7+}$ to form $[Mn_xAl_{13-x}O_4(OH)_{24}(OH_2)_{12}]^{(7-x)+}$,[38] which under heating initiation, avoids the occurrence of redox reaction between Mn^{2+} and $S_2O_8^{2-}$ to form black MnO_2 nanoparticles.

It is known that charge storage mechanism of $LiMn_2O_4$ cathode is based on Li^+ intercalation/de-intercalation into lattice.[37] We firstly prepared DPH containing Li^+, Zn^{2+} and Mn^{2+}, i.e., DPH(LiZnMn). Electrochemical performances of Zn//$LiMn_2O_4$ based on DPH(LiZnMn) polyelectrolyte are evaluated. As shown in Figure S32a (Supporting Information), Zn//$LiMn_2O_4$ in the voltage window of 0.2–2.55 V exhibits a cycling process composed of activation for 0–20 cycles and capacity increase for 21–200 cycles at 0.5 C. After 200 cycles, the capacity is up to 113 mAh g^{-1}. The second charge/discharge curve exhibits low coulombic efficiency (≈65% = 228/351). The 31–40 discharge/charge presents much improved coulombic efficiency (≈86% = 38.8/45). The electrochemical properties are poor. Thus, we focus on the possibility of Na^+ storage in $LiMn_2O_4$.

Na^+ and Zn^{2+} conducting DPH(CZnMn) polyelectrolyte make Zn//$LiMn_2O_4$ coin cell generate better electrochemical properties in Figure S33 (Supporting Information). As a control polyelectrolyte, PH is soaked into aqueous solution containing Na^+, Zn^{2+}, Mn^{2+}, and SO_4^{2-} to obtain Na^+ and Zn^{2+} as well as SO_4^{2-} conducting PH. The initial two charge/discharge curves are collected to evaluate the possibility of Zn//$LiMn_2O_4$ coin cell operating in the voltage window of 0.2–2.8 V. For Zn//$LiMn_2O_4$ based on DPH(CZnMn) in Figure S33b (Supporting Information), the limit of cathode charging voltage is up to 2.55 V, higher than that of coin cell based on control polyelectrolyte (2.26 V). The discharge capacity of Zn//$LiMn_2O_4$ based on DPH(CZnMn) is ≈300 mAh g^{-1}, but no discharge capacity is observed for coin cell based on control polyelectrolyte. DPH(CZnMn) polyelectrolyte can make Zn//$LiMn_2O_4$ coin cell operating in higher cathodic voltage limiting, contributing to higher energy (density). Zn//$LiMn_2O_4$ coin cell based on DPH(CZnMn) is tested in the optimized voltage window of 0.2–2.3 V. And corresponding charge/discharge curves at 2.6 C exhibit high coulombic efficiency of ≈100% in Figure S33c (Supporting Information). High capacity of 270 mAh g^{-1} is obtained at 0.15 C, and excellent rate capability is also got (e.g., 130 mAh g^{-1} at 20 C), which is superior to Zn//$LiMn_2O_4$ based on DPH(LiZnMn) polyelectrolyte. Zn//$LiMn_2O_4$ coin cell based on DPH(CZnMn) exhibits excellent long-term cycling stabilities (e.g., 174 mAh g^{-1} at 0.85 C) in Figure S33(e,f) (Supporting Information). Nyquist plots are introduced to evaluate the impedance change of coin cell. After long-term cycles, much decreased charge transfer resistance (*Rct*)

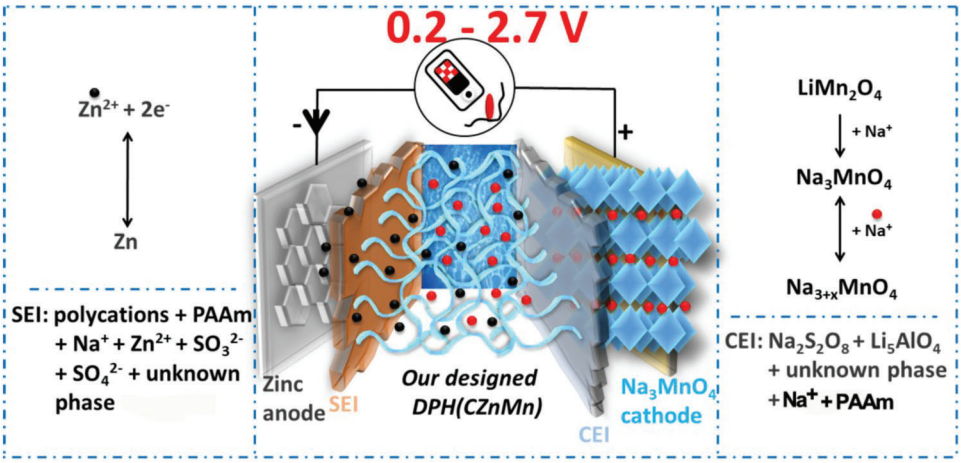

Figure 3. Schematic diagram of charge storage mechanism for Zn//$LiMn_2O_4$ base on DPH(CZnMn).

is present as shown in Figure S33g (Supporting Information). Zn//$LiMn_2O_4$ before and after cycling exhibit semicircle in the enlarged high-frequency part, which is due to the formation of SEI and/or CEI.

Charge storage mechanism of Zn//$LiMn_2O_4$ based on DPH(CZnMn) is uncovered. As shown in Figure S34a (Supporting Information), the shape of initial two charge/discharge curves is different from third and fourth ones. Charge storage process of $LiMn_2O_4$ cathode is elucidated firstly using Raman spectroscopy, XRD, and SEM. Due to the strong adhesion between DPH(CZnMn) and $LiMn_2O_4$ cathode after charging/discharging test, a mass of active material adhered to DPH(CZnMn) surface is used for Raman and XRD characterizations. As shown in Figure S34b (Supporting Information), Raman spectrum exhibits a characteristic band at ≈623 cm^{-1} corresponding to Mn–O symmetric stretching vibration in MnO_6 octahedral.[39] Compared to pristine 623 cm^{-1}, the total changed Raman wavenumber of second charge/discharge process is up to +19 cm^{-1}, indicating large irreversibility of lattice distortion in MnO_6 octahedron. Compared to pristine 623 cm^{-1}, the total changed Raman wavenumber of fourth charge/discharge process is +1 cm^{-1}, indicating large reversibility of lattice distortion in MnO_6 octahedron. XRD patterns are collected to uncover the phases of active materials at different charge/discharge states as shown in Figure S34c (Supporting Information). Severe phase transitions occur during the initial two charge/discharge tests, pristine $LiMn_2O_4$ phase and Na^+ in DPH(CZnMn) transforms into $Na_2Mn_5O_{10}$ (PDF#27-0749) and Na_3MnO_4 (PDF#32-1126) phases. The formed $Na_2Mn_5O_{10}$ and Na_3MnO_4 become active materials during the following charge/discharge tests, which is demonstrated by XRD pattern of fourth charge/discharge in Figure S34c (Supporting Information). Charge storage mechanism of Na_3MnO_4 is based on Na^+ intercalation/de-intercalation demonstrated by diffraction peaks shift (i.e., (120), (101), and (021)), as shown in Figure S34c (Supporting Information). Charge storage mechanism of $Na_2Mn_5O_{10}$ is through conversion reaction demonstrated by the appear and disappear of diffraction peaks (i.e., (201)), as shown in Figure S34c (Supporting Information). During the four charge/discharge tests, inorganics (i.e., $Na_2S_2O_8$ (PDF#01-0664), Li_5AlO_4 (PDF#24-0596)) are detected and as one of CEI compositions. $Na_2S_2O_8$ is derived from the reaction ($2Na^+ + SO_4^- + SO_4^- = Na_2S_2O_8$), in which sulfate radicals (SO_4^-) can generate in the transformation process of aluminum polycations in Figure S19b (Supporting Information). Li_5AlO_4 may be derived from reaction of Li^+ and aluminum polycations, e.g., $[AlO_4Al_{12}(OH)_{24}(OH_2)_{12}]^{7+}$. SEM measurement is carried out to observe the CEI of residual CEI/active materials on carbon black/carbon cloth(current collector). Some residual active materials distribute on surface of current collector, as shown in Figure S34e (Supporting Information). After search in patience, CEI is found and exhibits smooth surface, as shown in Figure S34f (Supporting Information). From the edge of cracked CEI in Figure S34g (Supporting Information), we observe that CEI is coated on the surface of active materials.

Charge storage mechanism of zinc anode in Zn//$LiMn_2O_4$ based on DPH(CZnMn) is investigated. Zinc foil anode after charge/discharge test exhibits smooth surface in Figure S35a (Supporting Information). SEI is observed from cross-section diagram in Figure S35b (Supporting Information). Excluding zinc metal phase, no obvious basic zinc sulfate phase is detected as shown in Figure S35c (Supporting Information). XPS measurement is carried out to detect SEI composition on the surface of zinc anode, as shown in Figure S36 (Supporting Information). SEI is composed of polyacrylamide and aluminum polycations derivatives, which is the same as SEI of zinc anode in Zn//Zn symmetric coin cell.

Charge storage mechanism of Zn//$LiMn_2O_4$ based on DPH(CZnMn) is as shown in **Figure 3**, Charge storage of cathode through phase transition is based on Na^+ intercalation/de-intercalation (Na_3MnO_4) and conversion reaction ($Na_2Mn_5O_{10}$). CEI consists of inorganics ($Na_2S_2O_8$, Li_5AlO_4, and unknown phases) and organics (polyacrylamide derivative). Zinc anode stores charge through zinc plating/stripping. SEI consists of inorganics and organics (aluminum polycations and polyacrylamide derivatives) as well as unknown phase. Interphases at interfaces of electrode/DPH(CZnMn) are from the polymerization of residual acrylamide monomer initiated by developed initiator system, not related to HOMO and LUMO of polyacrylamide.[21] The unknown phase is substances may containing isocyanic

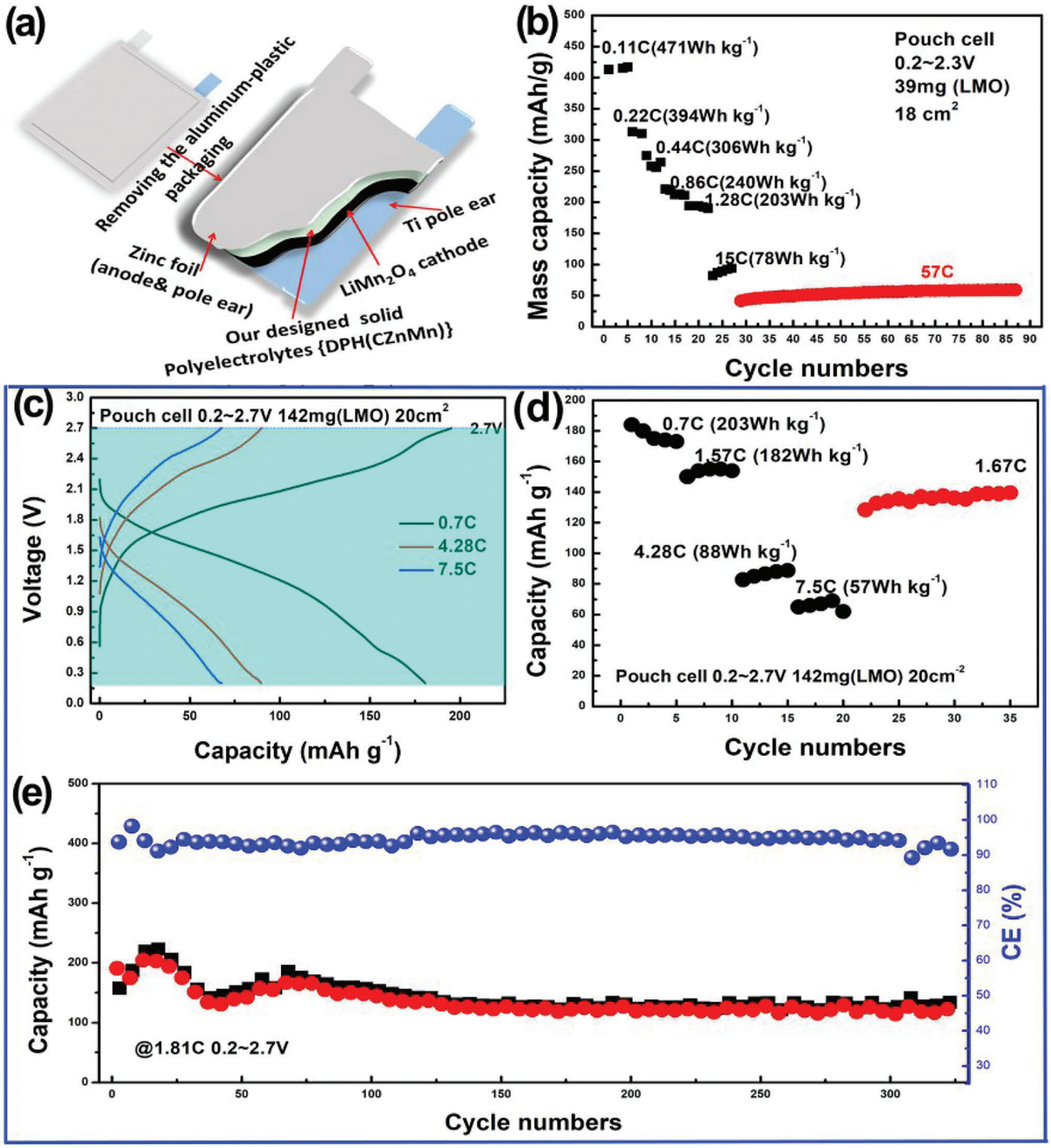

Figure 4. Electrochemical properties of Zn//$LiMn_2O_4$ pouch cell based on DPH(CZnMn) polyelectrolyte. a) Schematic diagram of pouch cell. b) Rate capability of pouch cell with mass loading of ≈2.17mg$LiMn_2O_4$ cm^{-2} and voltage window of 0.2–2.3 V. c) GCD curves, d) rate capability, and e) long-term cycling stability of pouch cell with mass loading of ≈7.1 mg$LiMn_2O_4$ cm^{-2} and voltage window of 0.2–2.7 V.

acid and cyanate group.[16] Active carbon cloth-based symmetric solid-state supercapacitor based on PDH(CZnMn) can operate in voltage window of 0–2.5 V, and exhibits ≈98% initial capacitance retention after 10 000 cycles at 30 mA cm^{-2}, as shown in Figure S37a (Supporting Information). CV and charge/discharge curves of the supercapacitor show electric double layer behavior in Figure S37b,c (Supporting Information). SEI and/or CEI are observed in Nyquist plot of the cycled supercapacitor in Figure S37d (Supporting Information). Except from decreased content of free water, in situ formed SEI and CEI mainly contributes to the tolerance of low-concentrated aqueous DPH-based polyelectrolytes to high-voltage window.

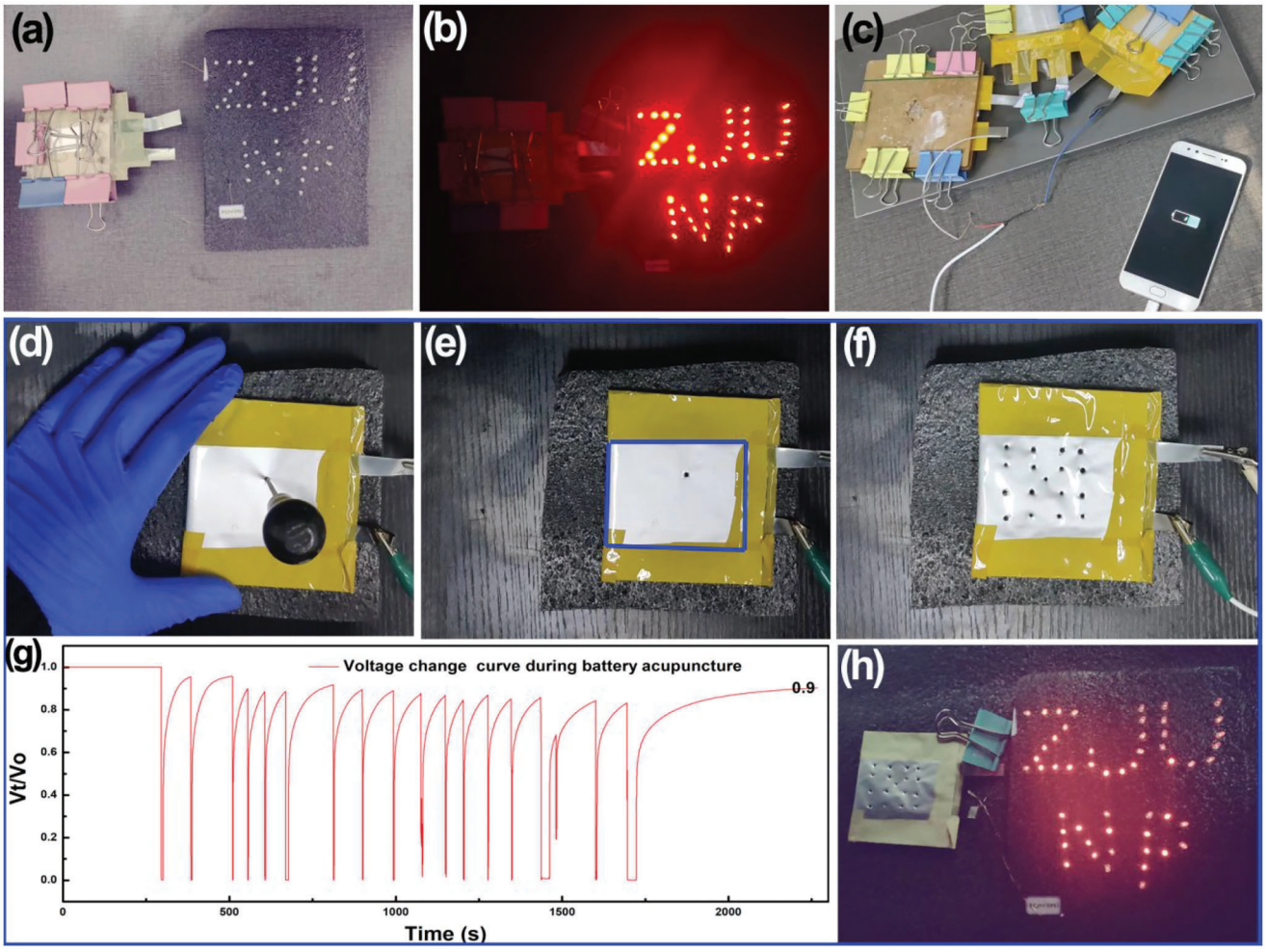

Figure 5. Applications of $Zn//LiMn_2O_4$ pouch cell as power source. a,b) Fifty red LEDs in parallel lightened by a $Zn//LiMn_2O_4$ pouch cell. c) Mobile phone charged by three $Zn//LiMn_2O_4$ pouch cells in series. d–f) Acupuncture experiments on $Zn//LiMn_2O_4$ pouch cell. g) Variations of the acupuncture voltage versus the initial voltage during acupuncture experiments. h) Fifty red LEDs in parallel lightened by a charged acupuncture $Zn//LiMn_2O_4$ pouch cell.

2.4. Safe, High-Energy $Zn//LiMn_2O_4$ Pouch Cell Based on DPH(CZnMn) Polyelectrolyte

Large-size DPH(CZnMn) polyelectrolyte is prepared in Figure S38a (Supporting Information). Pouch cell is assembled as shown in **Figure 4**a and Figure S38b (Supporting Information). Electrochemical properties of $Zn//LiMn_2O_4$ pouch cell with mass loading of ≈2.17mg$LiMn_2O_4$ cm^{-2} are assessed first in the operating voltage window of 0.2–2.3 V. As shown in Figure S38c (Supporting Information) and Figure 4b, specific capacity and corresponding energy density are up to ≈410 mAh g^{-1} and ≈471 Wh kg^{-1} at 0.11 C, respectively. ≈50 mAh g^{-1} capacity is still obtained at 57 C, indicating a high rate capability. After ≈240 cycles at 0.35 C, specific capacity is up to ≈300 mAh g^{-1} in Figure S38d (Supporting Information), demonstrating excellent cycling stability. Electrochemical properties of $Zn//LiMn_2O_4$ pouch cell with mass loading of ≈7.1mg$LiMn_2O_4$ cm^{-2} are assessed second in the operating voltage window of 0.2–2.7 V. As shown in GCD curves of Figure 4c, DPH(CZnMn) polyelectrolyte can make $Zn//LiMn_2O_4$ pouch cell charge to 2.7 V at different rates. As shown in Figure 4d, specific capacity and energy density are up to ≈180 mAh g^{-1} and 203 Wh kg^{-1} at 0.7 C, respectively. ≈70 mAh g^{-1} capacity can be obtained at 7.5 C, indicating excellent rate capability. Long-term cycling stability in the voltage window of 0.2–2.7 V is evaluated as shown in Figure 4e, and above 90% initial capacity is kept after 320 cycles at 1.81 C. Nyquist plot of pouch cell after cycles exhibits SEI and CEI are in situ formed as shown in Figure S38e (Supporting Information), which improves the tolerance of DPH-based polyelectrolytes to high voltage.

As shown in **Figure 5**a,b, 50 red LEDs in parallel are lightened by $Zn//LiMn_2O_4$ pouch cell charged to 2.7 V for ≈12 h. A mobile phone can be charged by three $Zn//LiMn_2O_4$ pouch cells in series in Figure 5c. As shown in Figure 5d–f, a fully charged $Zn//LiMn_2O_4$ pouch cell is acupunctured many times to demonstrate its safety. Combustion and smoke are not observed during the acupuncture experiments (Video S1, Supporting Information). And DPH hydrogel polyelectrolyte exhibits flame

retardancy (Video S2, Supporting Information). The open circuit voltage decreases into ≈0 V when a steel needle with 2 mm diameter acupunctures into pouch cell, and can recover to ≈95% initial open circuit voltage within short time when pulled out. Variations of the acupuncture voltage versus the initial open circuit voltage during acupuncture experiments are collected as shown in Figure 5g, and the open circuit voltage can recover to ≈90% initial open circuit voltage within 550 s after 17th acupuncture. 50 red LEDs in parallel can be still lightened by an acupunctured $Zn//LiMn_2O_4$ pouch cell charged to 2.7 V. A red LED can be lightened by three self-generating cells in series in dark, as shown in Figure S39 (Supporting Information), where a self-generating cell is composed of a piece of DPH(CZnMn) polyelectrolyte with area of 4×5 cm^2 sandwiched by zinc foil anode and titanium foil cathode.

3. Conclusion

High-voltage low-concentration polyacrylamide hydrogel polyelectrolyte with high ionic conductivity is prepared by our developed initiator system (aluminum polycations). The designed polyacrylamide hydrogel polyelectrolyte exhibits above 3.5 V electrochemical stability window and ≈280 mS cm^{-1} ionic conductivity at 25°C. The developed aluminum polycations as cross-linking agent can both generate radicals to initiate acrylamide monomers to form hydrogel and produce free radical to initiate residual acrylamide monomers to in situ form interphases (i.e., SEI and CEI) at interfaces of electrode/hydrogel polyelectrolyte in assembled batteries. This widens electrochemical stability window of hydrogel polyelectrolyte and aqueous $zinc//LiMn_2O_4$. Al^{3+} as hard Lewis acid accepts Lewis base (e.g., SO_4^{2-} and OH^- as well as H_2O) to form aluminum polycations interacting with amide groups, forming single ion conductor. And this contributes to high ionic conductivity. The designed hydrogel polyelectrolyte makes $Zn//LiMn_2O_4$ pouch cell (2.2 mg cm^{-2}, $LiMn_2O_4$) operate in the voltage window of 0.2–2.3 V, exhibiting high energy density (471 Wh $kg_{LiMn2O4}{}^{-1}$) and excellent cycling stability (300 mAh g^{-1} after 240 cycles at 0.35 C) as well as high rate capability (410 mAh g^{-1} at 0.11 C; 50 mAh g^{-1} at 57 C). Also, the designed hydrogel polyelectrolyte can make $Zn//LiMn_2O_4$ pouch cell (7.1 mg cm^{-2}, $LiMn_2O_4$) operate in the voltage window of 0.2–2.7 V, delivering high energy density (203 Wh $kg_{LiMn2O4}{}^{-1}$) and excellent cycling stability (145 mAh g^{-1} after 320 cycles at 1.81 C) as well as good rate capability (175 mAh g^{-1} at 0.7 C; 70 mAh g^{-1} at 7.5 C). Full charged pouch cells can lighten 50 red LEDs in series and charge a cellphone. Combust and smoke are not observed in the battery acupuncture experiment. A red LED can be lightened by self-generating cells that a self-generating cell is composed of a piece of DPH(CZnMn) polyelectrolyte sandwiched by zinc foil anode and titanium foil cathode.

Supporting Information

Supporting Information is available from the Wiley Online Library or from the author.

Acknowledgements

The authors thank the staff member Haiwen Lai of Hangzhou Gaoxi Technology Co., LTD for helping assemble pouch cells. This work was supported by the National Natural Science Foundation of China (No. 52090030), the Fundamental Research Funds for the Central Universities (No. 2021FZZX001-17) and Shanxi-Zheda Institute of New Materials and Chemical Engineering (No. 2022SZ-TD011, 2022SZ-TD012, 2022SZ-FR004).

Conflict of Interest

The authors declare no conflict of interest.

Author Contributions

T.Q. and C.G. conceived the idea for the project. T.Q. prepared the materials, performed the electrochemical experiments, conducted the characterizations and the manuscript. K.L., Y.L., and Z.X. took part in discussion on research content.

Data Availability Statement

Research data are not shared.

Keywords

controlled/active initiation system, high-voltage zinc-based pouch cells, low-concentration hydrogel polyelectrolytes, in-situ formed interphases, wide electrochemical window

Received: March 9, 2023
Revised: April 6, 2023
Published online:

[1] S. Zhang, T. Liang, D. Wang, Y. Xu, Y. Cui, J. Li, X. Wang, X. Xia, C. Gu, J. Tu, *Adv. Sci.* **2021**, *8*, 2003241.
[2] P. Sun, R. Bisschop, H. Niu, X. Huang, *Fire Technol.* **2020**, *56*, 1361.
[3] K. Xu, *Chem. Rev.* **2014**, *114*, 11503.
[4] Y. Liang, Y. Yao, *Nat. Rev. Mater.* **2022**,*8*, 109.
[5] Y. S. Meng, V. Srinivasan, K. Xu, *Science* **2022**, *378*, abq3750.
[6] L. Yuan, J. Hao, C.-C. Kao, C. Wu, H.-K. Liu, S.-X. Dou, S.-Z. Qiao, *Energy Environ. Sci.* **2021**, *14*, 5669.
[7] H. Chen, J. Huang, S. Tian, L. Liu, T. Qin, L. Song, Y. Liu, Y. Zhang, X. Wu, S. Lei, S. Peng, *Adv. Sci. (Weinh)* **2021**, *8*, 2004924.
[8] Z. Cai, Y. Ou, J. Wang, R. Xiao, L. Fu, Z. Yuan, R. Zhan, Y. Sun, *Energy Storage Mater.* **2020**, *27*, 205.
[9] L. Cao, D. Li, T. Pollard, T. Deng, B. Zhang, C. Yang, L. Chen, J. Vatamanu, E. Hu, M. J. Hourwitz, L. Ma, M. Ding, Q. Li, S. Hou, K. Gaskell, J. T. Fourkas, X.-Q. Yang, K. Xu, O. Borodin, C. Wang, *Nat. Nanotechnol.* **2021**, *16*, 902.
[10] J. Yan, E. H. Ang, Y. Yang, Y. Zhang, M. Ye, W. Du, C. C. Li, *Adv. Funct. Mater.* **2021**, *31*, 2010213.
[11] W. Du, E. H. Ang, Y. Yang, Y. Zhang, M. Ye, C. C. Li, *Energy Environ. Sci.* **2020**, *13*, 3330.
[12] C. Dong, F. Xu, L. Chen, Z. Chen, Y. Cao, *Small Struct.* **2021**, *2*, 2100001.
[13] S. Chen, R. Lan, J. Humphreys, S. Tao, *ACS Appl. Energy Mater.* **2020**, *3*, 2526.
[14] Q. Ni, B. Kim, C. Wu, K. Kang, *Adv. Mater.* **2022**, *34*, 2108206.
[15] J. Zhao, J. Zhang, W. Yang, B. Chen, Z. Zhao, H. Qiu, S. Dong, X. Zhou, G. Cui, L. Chen, *Nano Energy* **2019**, *57*, 625.

[16] X. Hou, R. Wang, X. He, T. P. Pollard, X. Ju, L. Du, E. Paillard, H. Frielinghaus, L. C. Barnsley, O. Borodin, K. Xu, M. Winter, J. Li, *Angew. Chem., Int. Ed.* **2021**, *60*, 22812.
[17] X. Hou, T. P. Pollard, W. Zhao, X. He, X. Ju, J. Wang, L. Du, E. Paillard, H. Lin, K. Xu, O. Borodin, M. Winter, J. Li, *Small* **2022**, *18*, 2104986.
[18] G. Odian, *Principles of polymerization*, John Wiley & Sons, New York **2004**.
[19] A. Ravve, *Principles of polymer chemistry*, Springer Science & Business Media, Berlin **2013**.
[20] D. Zhao, S. Li, *Front Chem* **2020**, *8*, 821.
[21] J. B. Goodenough, Y. Kim, *Chem. Mater.* **2009**, *22*, 587.
[22] J. B. Goodenough, *Nat. Electron.* **2018**, *1*, 204.
[23] C. Ye, Z. Bi, D. Wang, *Colloids Surf., A* **2013**, *436*, 782.
[24] W. H. Casey, B. L. Phillips, G. Furrer, *Rev Mineral Geochem* **2001**, *44*, 167.
[25] R. J. Stol, A. K. Van Helden, P. L. De Bruyn, *J. Colloid Interface Sci.* **1976**, *57*, 115.
[26] H. De Hek, R. J. Stol, P. L. De Bruyn, *J. Colloid Interface Sci.* **1978**, *64*, 72.
[27] J. E. Van Benschoten, J. K. Edzwald, *Water Res.* **1990**, *24*, 1519.
[28] S. Bi, *Coord. Chem. Rev.* **2004**, *248*, 441.
[29] V. G. Gaikar, K. V. Padalkar, V. K. Aswal, *J. Mol. Liq.* **2008**, *138*, 155.
[30] M. Zhu, X. Wang, H. Tang, J. Wang, Q. Hao, L. Liu, Y. Li, K. Zhang, O. G. Schmidt, *Adv. Funct. Mater.* **2019**, *30*, 1907218.
[31] E. H. Hygh, R. M. Welch, *Phys. Rev. B* **1970**, *1*, 2424.
[32] X. Lu, C. Y. Chan, K. I. Lee, P. F. Ng, B. Fei, J. H. Xin, J. Fu, *J. Mater. Chem. B* **2014**, *2*, 7631.
[33] J. L. Yang, J. Li, J. W. Zhao, K. Liu, P. Yang, H. J. Fan, *Adv. Mater.* **2022**, *34*, 2202382.
[34] M. Zhou, C. Fu, L. Qin, Q. Ran, S. Guo, G. Fang, X. Lang, Q. Jiang, S. Liang, *Energy Storage Mater.* **2022**, *52*, 161.
[35] W. Deng, Z. Xu, X. Wang, *Energy Storage Mater.* **2022**, *52*, 52.
[36] H. Liu, J.-G. Wang, W. Hua, L. Ren, H. Sun, Z. Hou, Y. Huyan, Y. Cao, C. Wei, F. Kang, *Energy Environ. Sci.* **2022**, *15*, 1872.
[37] T. Zhang, Y. Tang, G. Fang, C. Zhang, H. Zhang, X. Guo, X. Cao, J. Zhou, A. Pan, S. Liang, *Adv. Funct. Mater.* **2020**, *30*, 2002711.
[38] J. Kudynska, H. A. Buckmaster, K. Kawano, S. M. Bradley, R. A. Kydd, *J. Chem. Phys.* **1993**, *99*, 3329.
[39] J. Li, N. Luo, L. Kang, F. Zhao, Y. Jiao, T. J. Macdonald, M. Wang, I. P. Parkin, P. R. Shearing, D. J. L. Brett, G. Chai, G. He, *Adv. Energy Mater.* **2022**, *12*, 2201840.